water

MDPI

Article

Hydrological Dynamics of Debris Flow-Prone Pyroclastic Catchments: A Budyko-Based Modeling Approach

Muhammad Aleem, Pasquale Marino and Roberto Greco *

Dipartimento di Ingegneria, Università degli Studi della Campania 'Luigi Vanvitelli', Via Roma 29, 81031 Aversa, CE, Italy; muhammad.aleem@unicampania.it (M.A.); pasquale.marino1@unicampania.it (P.M.)
* Correspondence: roberto.greco@unicampania.it

Abstract

Rainfall-induced geohazards in pyroclastic slopes are known to be influenced by antecedent soil wetness, but the assessment of this condition based on the catchment water balance is still unexplored. A lumped Dynamic Water Balance Model (DWBM) based on the Budyko framework is developed to characterize the hydrological behavior of eight landslide-prone catchments underlain by pyroclastic deposits over limestone bedrock in Campania, Italy. Using monthly rain-gauge, satellite, and reanalysis data between 2003 and 2023, model parameters representing catchment retention, evapotranspiration efficiency, maximum soil storage, baseflow response, and groundwater losses were calibrated against the discharge, estimated from reanalysis runoff, for seven ungauged catchments and from a stage–discharge relationship for one gauged catchment. This allowed an assessment of the consistency of reanalysis runoff for setting up hydrological models of ungauged catchments. During calibration, the models reproduced discharge satisfactorily (RMSE = 11.66–25.95 mm; NNSE = 0.80–0.90; KGE = 0.76–0.91), although the performance decreased in some catchments in model validation (RMSE = 13.60–28.97 mm; NNSE = 0.61–0.92; KGE = 0.55–0.91). Monte Carlo and Sobol analyses revealed distinct parameter sensitivities, with evapotranspiration efficiency, catchment retention, and maximum soil storage contributing directly to model output variability, while groundwater-related parameters were primarily influential through interactions with other parameters. Physically interpretable relationships of model parameters with catchment characteristics were found, allowing a hydrological characterization of poorly gauged pyroclastic catchments. Modeled soil storage provides a physically meaningful proxy for antecedent slope wetness, potentially supporting the assessment of rainfall-induced geohazards.

Keywords: Budyko framework; rainfall-induced landslides; morphometric parameters; water balance; ungauged catchments; ERA5-Land; TerraClimate

Check for updates

Academic Editor: Achim A. Beylich

Received: 21 September 2026
Revised: 19 October 2026
Accepted: 21 October 2026
Published: 23 October 2026

Copyright: © 2026 by the authors. Licensee MDPI, Basel, Switzerland. This article is an open access article distributed under the terms and conditions of the Creative Commons Attribution (CC BY) license.

1. Introduction

Hydrological modeling plays a key role in water resource management and in understanding processes such as precipitation, infiltration, runoff, and evaporation, allowing the prediction of streamflow, groundwater recharge, and the assessment of land use impact [1]. These processes are also crucial for the assessment and management of geo-hazards induced by rainfall, such as floods and landslides, which can cause significant damage to both infrastructure and human life globally. Assessing the water balance may help identify the influence of various hydrological processes on the establishment of predisposing conditions for the occurrence of geo-hazards.

A water balance assessment can be carried out with different modeling approaches [2,3], spanning physically based distributed or semi-distributed models, conceptual lumped models, and, more recently, machine learning models [4,5]. Comparative studies have shown that lumped hydrological models can perform competitively with distributed and semi-distributed models, particularly for water balance and runoff simulations [6–8]. Basically, in data-scarce catchments, lumped models can be effectively used to understand hydrology without extensive input requirements [9]. Indeed, assessing the water balance components using lumped models offers several advantages. First, it allows for the quantification of the amount of water available in a catchment, which directly impacts the hydrological conditions of slopes [10]. Second, it helps understand the influence of different climatic conditions on the water balance. Third, it provides valuable insights into the impact of rainfall events, runoff, and vegetation on evapotranspiration, which is crucial for assessing the effect of global warming on catchment hydrology [11]. The Budyko model, developed by M.I. Budyko in the mid-20th century, is one of the most widely used frameworks for studying the long-term water balance in a catchment with a lumped approach [12]. A Budyko-based Dynamic Water Balance Model (DWBM) was developed to analyze the water balance at annual and smaller scales by considering the impact of water storage [13]. DWBM can be applied to understand the interaction of climate conditions and vegetation patterns with all terms of the water balance, such as soil storage, actual evapotranspiration, runoff, and groundwater storage.

Recent research continues to apply lumped models for diverse purposes [14,15], but they are still rarely applied to determine hydrologic conditions predisposing catchments to geohazards [16]. Limited ground data makes it difficult to analyze the hydrological processes occurring in slopes. Thus, remote sensing and reanalysis products offer an alternative option for hydrological modeling in ungauged catchments. They capture the spatial and temporal variability of hydrometeorological variables needed to understand landslide occurrences. In this respect, hydrological models can be calibrated using remote sensing and reanalysis data to simulate hydrological variables for geohazard studies.

The Campania region, southern Italy, is frequently hit by shallow rainfall-induced landslides and debris flows, affecting steep slopes covered by loose granular volcanoclastic deposits, often overlying a karstic limestone fractured bedrock [17–19]. The volcanoclastic deposits (like ash, pumice, and lapilli) exhibit peculiar properties compared to other soils. In fact, these deposits allow rapid infiltration and can temporarily store much water owing to their high porosity. However, they have relatively limited water retention owing to the prevailing coarse-grained fraction in their texture [20]. This leads to high variability in soil moisture and runoff [21]. Although many studies indicate that the occurrence of geohazards in this area is strongly influenced by antecedent conditions (e.g., [18,22,23]), their assessment of soil storage dynamics at a catchment scale has never been carried out.

In this paper, the water balance of landslide-prone catchments in Campania is modeled with a lumped approach based on the Budyko framework, by exploiting data from different sources, including both ground-based and satellite data between 2003 and 2023. Specifically, catchments with and without a stream gauge station at the outlet have been analyzed, to assess if satellite and reanalysis products can supplement ground data in ungauged catchments. Moreover, catchment geomorphologic characteristics that can affect hydrological processes [24–26] have been also investigated. Finally, a sensitivity analysis of the model to parameter variations has been carried out to identify, which among catchment features, exert the strongest control on the water balance. Overall, the objectives of this study are as follows: (a) to evaluate water balance components controlling the response to intense precipitation in eight pyroclastic catchments; (b) to assess the consistency of satellite and reanalysis data for water balance modeling in ungauged catchments; (c) to

investigate the influence of catchment geomorphology on model parameters; (d) to explore model parameter uncertainty across multiple catchments through Monte Carlo sampling and Sobol sensitivity analysis.

2. Materials and Methods

2.1. Study Area

This study examines eight catchments with diffuse pyroclastic soil deposits located in Campania (Southern Italy) (Figure 1), characterized by a diverse landscape including fertile plains, the Apennine Mountains, and coastal zones along the Tyrrhenian Sea. The climate is Mediterranean with hot, dry summers and mild, wet winters [27]. Mean annual rainfall varies between 1000 and 1800 mm, while potential evapotranspiration ranges between 600 and 1000 mm, depending on the altitude. On average, the precipitation regime is characterized by a dry season (from May/June to September) and a wet season (from October to the end of April/May) [21]. The terrain is characterized by layers of loose pyroclastic materials, including volcanic ash, pumice, and lapilli, which create a porous and unstable soil [20]. The deposits are characterized by very high porosity, up to 75% in the ash layer [28], and a thickness of a few meters [29]. The loose, unconsolidated nature of pyroclastic materials, specifically on the steepest slopes, contributes to the region's susceptibility to erosion and landslides, especially during intense rainfall. Understanding the interactions among precipitation (P), evapotranspiration (ET), runoff (Q), and subsurface storage is essential for assessing slope instabilities and debris floods.

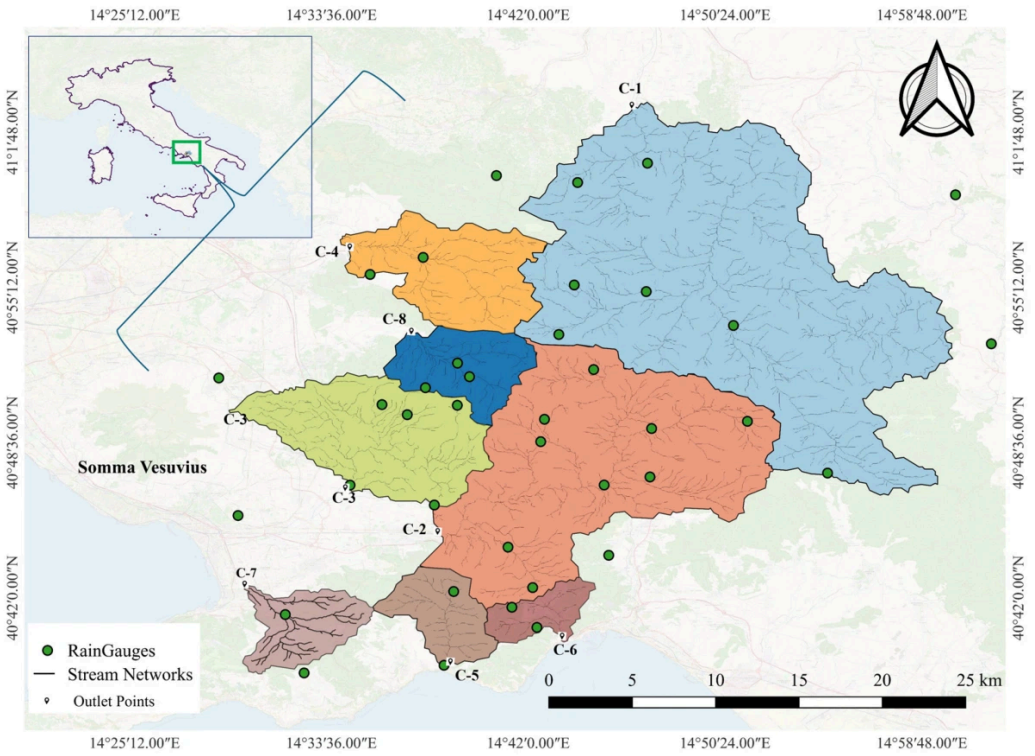


Figure 1. Location of the eight pyroclastic catchments in Campania, southern Italy. The map shows the catchment boundaries (C1–C8), drainage network derived from the digital elevation model (DEM), and hydrometeorological stations used in the analysis.

Morphological characteristics of catchments may significantly influence hydrological processes such as runoff generation, infiltration, actual evapotranspiration, and groundwater recharge [30,31]. In this study, morphometric indices (Tables 1 and 2) were derived from a Digital Elevation Model (DEM) implemented in QGIS v3.44.14 to describe the

physical characteristics of catchments [32]. These parameters are used to characterize a catchment based on its size and shape and also considering the influence of the structure and density of the drainage network [33]. They depend on the geometric structure and terrain configuration of the watershed, which directly control the movement and storage of water within the catchment [34–36]. Owing to the diffuse pyroclastic deposits originating from eruptions of the Vesuvius volcano, the distance from its crater has also been included among catchment attributes (Table 1). Although several of the considered morphometric parameters are clearly correlated and bring the same information, all the parameters listed in Table 1 were retained in the analysis, aiming at capturing any possible relationship between the catchment morphometry and model parameters.

Table 1. Morphometric indices used to characterize the geomorphological features of the study catchments along with their corresponding catchment characteristics.

Metric	Calculation Method	Catchment Characteristics
Total catchment area	A	Areal/Shape features
Catchment perimeter	P	
Circularity ratio	$Rc = \frac{4\pi A}{P^2}$	
Compactness coefficient (Ru)	$Ru = \frac{P}{2\sqrt{\pi A}}$	
Form factor	$Rf = \frac{A}{L^2}$	
Elongation ratio	$Ra = \frac{2}{\sqrt{\pi}}\sqrt{A}/L$	
Mean elevation	E_{mean}	Relief features
Mean slope	S	
Catchment relief	$H = E_{max} - E_{min}$	
Relief ratio	$R_h = \frac{H}{L}$	
Ruggedness index	$R_n = H \times D_d$	
Length of mainstream	L	Drainage network features
Total stream length	$L_{tot} = \sum L_s$	
Strahler order	U	
Drainage density	$D_d = \frac{L_{tot}}{A}$	
Distance from Vesuvius	D	Pyroclastic deposit thickness

Table 2. Calculated morphometric indices for the eight study catchments used to examine their relationship with the calibrated hydrological model parameters.

Metric	C1	C2	C3	C4	C5	C6	C7	C8
Mean Elevation (m)	609	420	158	556	498	391	571	589
Area (Sq.km)	429.7	245.5	98.9	74.5	32.5	19.1	42.3	33.7
Catchment perimeter (P) km	126.1	84.2	49.5	45.6	26.51	22.94	32.7	29.2
Mean slope (S)	0.201	0.229	0.086	0.205	0.430	0.278	0.278	0.398
Length of main stream (L_s) Km	41.5	26.5	8.3	12.7	7.5	5.3	8.1	7.4
Total stream length (km)	606.2	378.4	165.2	99.4	45.6	25.8	65.90	50.1
Circularity ratio (R_c)	0.34	0.43	0.51	0.45	0.58	0.46	0.50	0.50
Compactness coefficient (R_u)	1.72	1.52	1.40	1.49	1.31	1.48	1.42	1.42
Form factor (R_f)	0.25	0.52	1.43	0.47	0.58	1.12	0.64	0.62
Elongation ratio (R_a)	0.56	0.81	1.35	0.77	0.86	1.19	0.90	0.89
Strahler order (U)	5	5	5	4	3	4	4	4
Catchment relief (H) Km	1.61	1.57	1.12	1.42	1.29	1.10	0.98	1.38
Relief ratio (R_h)	0.04	0.07	0.13	0.11	0.17	0.26	0.12	0.19
Drainage density (D_d)	1.41	1.54	1.67	1.33	1.40	1.35	1.56	1.49
Ruggedness index (R_n)	2.27	2.42	1.87	1.89	1.81	1.48	1.53	2.05
Distance from Vesuvius (D) Km	25	22	10	14	12	18	9	12

2.2. Data Collection and Processing

Hydrometeorological data, including precipitation (P), potential evapotranspiration (ET_0), and runoff (Q), were collected at a monthly temporal scale for the selected catchments in Campania. Precipitation was obtained from 39 ground-based stations managed by the Civil Protection Agency of Campania (Figure 1 and Table 3), and inflow to catchments was estimated through the Thiessen polygons method [37]. The total study area is about 1000 km^2, and hence, each station covers a mean area of about 25 km^2.

Table 3. Coordinates of ground-based stations managed by the Civil Protection Agency of Campania (source: https://centrofunzionale.regione.campania.it/dati, accessed on 12 May 2026).

Station	Longitude	Latitude
Altavilla Irpina	14.78487674	41.00805025
Avellino Genio Civile	14.78398439	40.91707387
Cava dei Tirreni	14.7032051	40.70734718
Cetronico	14.70893401	40.81073544
Forino	14.74657369	40.86182128
Giffoni Valle Piana	14.9129665	40.78848531
Gragnano	14.52722423	40.68822978
Luogosano	15.00397053	40.98563121
Mercato S. Severino	14.75404291	40.78001317
Mercogliano	14.73275843	40.92174096
Monteforte Irpino	14.72181299	40.88665449
Ottaviano	14.47994078	40.85587361
Pellezzano	14.75731713	40.73022951
Piani di Prato	14.64958693	40.83651492
Pietrastornina	14.73517619	40.99435337
Pompei	14.4936146	40.75839953
Ponte Camerelle	14.68564451	40.73601128
Quindici	14.64972622	40.86637835
S. Martino Valle Caudina	14.67742942	40.99926887
S. Mauro	14.63325197	40.76584634
S. Pietro	14.78782137	40.82004212
Sarno	14.61398304	40.82984312
Serino	14.84601837	40.89306695
Solofra	14.85595931	40.82515604
Torriello	14.62692178	40.8489566
Tramonti	14.64701222	40.70456751
Visciano	14.58755955	40.92921336
Bracigliano	14.71159232	40.82659709
Quindici Torre Vecchia	14.65826013	40.85676493
Sarno (Acqued. Campano)	14.5960075	40.83698835
Mugnano Cardinale	14.62530968	40.94130524
Pizzolano	14.78662686	40.7857354
S. Marzano Sarno	14.57330307	40.77994585
Cava Casa Riceri	14.68842497	40.69341684
Cassano Irpino	15.02944	40.88008
Agerola METEO	14.54060925	40.64686174
Maiori	14.64014352	40.65228674
Cava Casa Riceri	14.68842497	40.69341684
Dragonea	14.70622949	40.67911264

Potential evapotranspiration (ET_0) was derived from the TerraClimate dataset at a 4 × 4 km spatial resolution, accessed via the Google Earth Engine (GEE). Discharge data availability varies among the catchments. Specifically, for the gauged catchment (C1), stream discharge (Q_o) was derived from observed water levels (h) using a stage–discharge

relationship developed from channel cross-sectional characteristics. For each recorded water level, the corresponding hydraulic radius was determined, and discharge was estimated using the Manning equation $Q = \left(\Sigma R^{2/3} s^{1/2}\right)/n$ [38], with the cross-section area (Σ) and hydraulic radius (R) calculated for the rectangular section of the river in the measurement section, and considering the slope (s = 0.06) and roughness of the channel of the river branch near the stream gauge operated by the Civil Protection. Manning's roughness coefficient $n = 0.04\ \mathrm{s/m^{1/3}}$ was assigned based on sporadic discharge estimates based on water velocity observed at the water surface. A sensitivity analysis was carried out to assess the uncertainty in the discharge calculation by varying Manning's roughness coefficient (n) ($\pm$20% of 0.04), the channel slope (s) ($\pm$10% of 0.06), and the daily water level (h) ($\pm$0.01 m). These ranges account for potential uncertainty in the channel roughness, slope estimation from topographic data, and water-level measurements, respectively. The water-level variation is also consistent with the maximum graduation error of $\pm$0.5 mm specified in the ISPRA technical guidelines (https://www.isprambiente.gov.it/it/pubblicazioni/manuali-e-linee-guida/files/mlg_60_2010.pdf, accessed on 18 October 2026). One hundred perturbed sets were randomly generated within the assumed ranges, and for each set, the entire series of mean monthly discharges was recalculated. The coefficient of variation (CV) of recalculated monthly discharges ranged from 11.68% to 13.13%, quantifying the combined uncertainty associated with the variations in the input parameters and showing limited variability.

Differently, for the ungauged catchments (C2 to C8), reanalysis-based discharge (Q_s) was estimated from the ERA5-Land dataset at a 9 × 9 km spatial resolution, also accessed through GEE. It is worth noting that these runoff data are not measured, but rather they are estimated with the surface hydrological module within a global atmospheric model, and that the assimilation of measurements during the reanalysis refers only to atmospheric variables. However, in ungauged catchments, only indirect information about runoff can be found. A detailed summary of the datasets collected for the study area is given in Table 4. For the gridded data from TerraClimate and ERA5-Land, the value for each catchment was calculated based on a weighted average based on the areas of the parts of the pixels of the grid belonging to each catchment. In every catchment, the period when all data were contemporarily available was used. The resulting datasets ranged between 14 and 20 years, in all cases long enough to get reliable model calibration and validation.

Table 4. Characteristics of the hydro-meteorological datasets used in this study for each catchment.

C. No	Variable	Observed Period	Spatial Resolution	Dataset	Source
C1 C2 C3–C4 C5–C8	Precipitation (P)	2003–2022 2009–2023 2009–2022 2008–2023	-	Ground stations	Civil Protection Agency
C1 C2 C3–C4 C5–C8	Potential Evapotranspiration (ET0)	2003–2022 2009–2023 2009–2022 2008–2023	4 × 4 km	Terra Climate	GEE
C1 C2 C3–C4 C5–C8	Runoff-Satellite (Qs)	2003–2022 2009–2023 2009–2022 2008–2023	9 × 9 km	ERA5-Land	GEE
C1	Runoff (Qo)	2003–2023		Stream gauge station	Civil Protection Agency

The overall methodological framework of this study is presented in Figure 2. Precipitation and ET_0 datasets collected for the selected catchments were used as inputs to a Budyko-based lumped hydrological model for each catchment. The models were calibrated and validated based on runoff at the outlet. Model parameters were analyzed in relation to catchment morphological features to investigate their influence on the hydrological response.

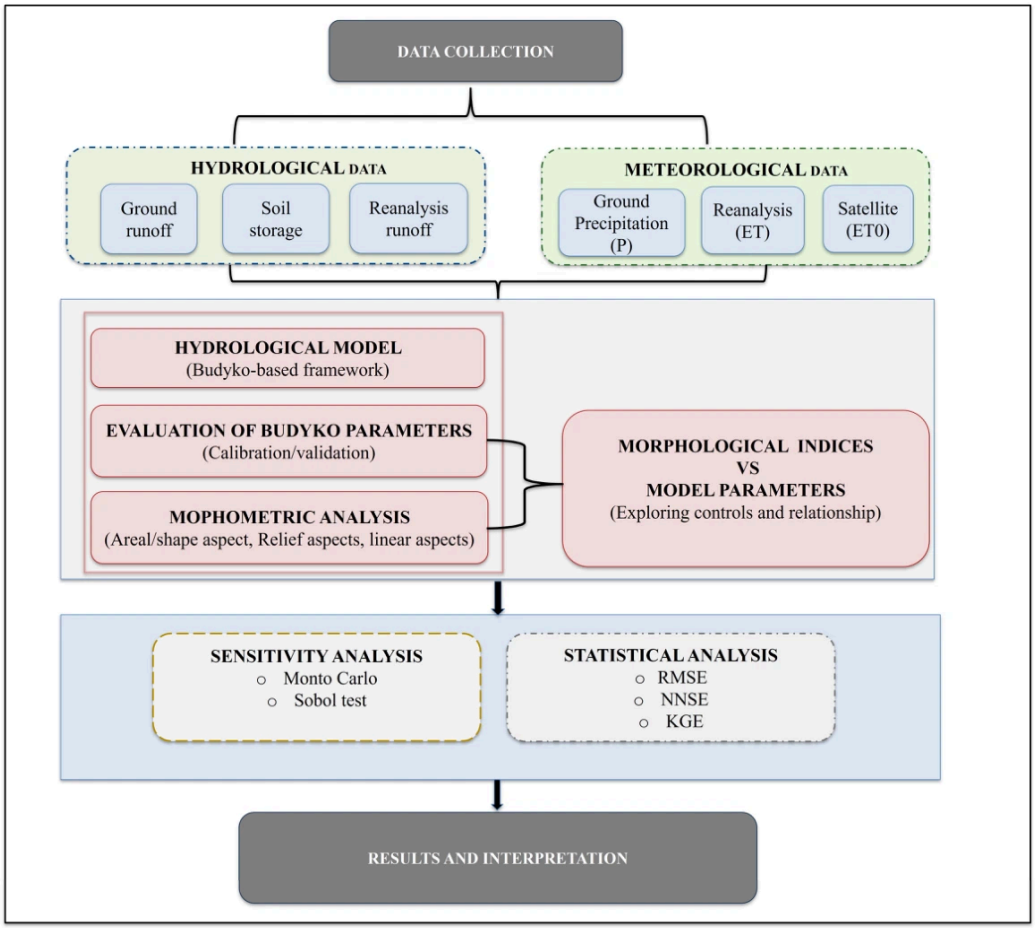


Figure 2. Schematic representation of the hydrological modeling framework based on the Budyko approach, showing the integration of hydrological and meteorological datasets, model parameter estimation, and subsequent statistical and sensitivity analyses for landslide-prone catchments.

2.3. Water Balance Modeling

2.3.1. Conceptual Budyko Framework

The Budyko framework [13] describes the long-term partitioning of precipitation (P) into actual evapotranspiration (ET) and runoff (Q) as a function of climatic aridity [39]. In this framework, evapotranspiration is controlled by two competing limits: water availability and atmospheric demand, represented by ET_0 [40]. While this framework is generally reliable for long-term averages in large catchments, its accuracy decreases for small basins and short-term time scales, where seasonal soil moisture fluctuations and groundwater dynamics are more pronounced [41]. To address these limitations, a Dynamic Water Balance Model was develop for sub-annual time scales using the supply–demand concept of the Budyko framework [42] and integrating soil moisture and groundwater flux to simulate the monthly water balance [12].

2.3.2. Dynamic Water Balance Model Based on Budyko Framework

In this study, a Dynamic Water Balance Model (DWBM) based on the Budyko concept is applied to simulate monthly hydrological processes in pyroclastic catchments. The DWBM represents catchment as two interacting storage components: soil storage (S) and aquifer storage (G). At each monthly time step, precipitation is partitioned into direct runoff (Q_d), ET, the soil storage change (ΔS), and groundwater recharge (R). The groundwater storage contributes to baseflow (Q_b), and deep groundwater representing loss form the system (Q_g), as reported by [18].

Figure 3 shows Fu's curve [43] (Equation (1)), which is used in [15] to calculate the value of a variable V between a supply limit V_s and a demand limit V_0.

$$\frac{V}{V_s} = 1 + \frac{V_0}{V_s} - [1 + \left(\frac{V_0}{V_s}\right)^{\frac{1}{1-\alpha}}]^{1-\alpha} \quad (1)$$

where $0 < \alpha < 1$ is a dimensionless parameter reflecting the effects of catchment characteristics such as vegetation, soil properties, and topography [40,44]. As parameter α increases, the curve approaches the limit, while it moves closer to the x-axis as α decreases.

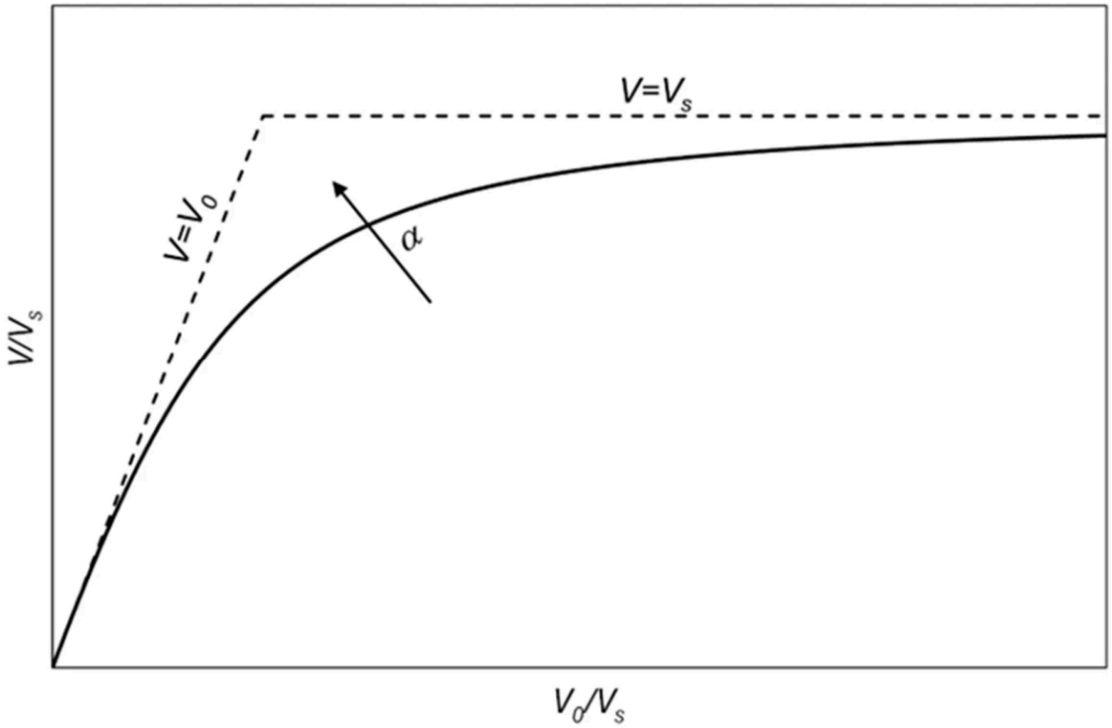


Figure 3. The curve and limit concept for water partitioning, including surface runoff and evapotranspiration in the DWBM.

By means of Equation (1), the catchment retention parameter α_1 is introduced to separate precipitation between direct runoff Q_d and catchment retention X. The closer α_1 is to the upper limit 1, the more the catchment retains precipitation without releasing direct runoff. In this case, the supply limit for X is the monthly precipitation P, and the demand limit X_0 is given by the sum of the available water storage capacity and potential evapotranspiration:

$$X_0 = [S_{max} - S_{m-1}] + ET_0 \quad (2)$$

Here, S_{max} is the maximum soil storage, and S_{m-1} is soil storage of the previous month. S_{max} is related to the thickness and porosity of soil deposits throughout the catchment. The retained water X is calculated using Equation (1), and direct runoff is readily obtained:

$$Q_d = P - X \tag{3}$$

Then, Fu's equation is applied again, introducing the evapotranspiration efficiency parameter α_2, to calculate the evapotranspiration opportunity Y, defined as the sum of soil storage and actual evapotranspiration [45]:

$$Y = S + ET \tag{4}$$

In this case, the demand limit is $Y_0 = S_{max} + ET_0$ and the supply limit is the water availability $W = S_{m-1} + X$.

With the same parameter α_2, Fu's equation is applied to calculate the actual evapotranspiration, for which the supply limit is again W, and the demand limit is ET_0.

Therefore, the parameter α_2 controls the fraction of retained water that is stored in the soil and then released as evapotranspiration.

At this stage, groundwater recharge R can be derived as the difference among water availability, soil storage, and evapotranspiration:

$$R = W - Y = W - S - ET \tag{5}$$

Finally, aquifer storage (G) is updated as follows:

$$G_m = G_{m-1} + R - Q_b - Q_g \tag{6}$$

In Equation (6), with a linear reservoir model of shallow groundwater, baseflow $Q_b = d \times G_{m-1}$ and deep groundwater recharge $Q_g = d_g \times G_{m-1}$ can be calculated.

Here, d and d_g represent the aquifer storage drainage coefficients, which control the release of groundwater to baseflow and to deep groundwater recharge, respectively.

Total runoff is finally computed as the sum of direct runoff (surface flow) and base flow (subsurface).

$$Q = Q_d + Q_b \tag{7}$$

The above-described model structure is represented in the flow chart of Figure 4, allowing a water balance assessment, provided that the values of parameters α_1, α_2, S_{max}, d, and d_g are assigned.

2.4. Model Calibration and Performance Evaluation

Model performance to reproduce the terms of the water balance, such as runoff Q, ET, and soil storage (S), was evaluated using various metrics (Table 5): Root Mean Square Error (RMSE); Kling–Gupta Efficiency (KGE); Normalized Nash–Sutcliffe Efficiency (NNSE); and the coefficient of determination (R^2) [46,47]. KGE evaluates the correlation, bias and variability simultaneously, providing an overall measure of model performance. NNSE measures the agreement between observed and simulated ranging between 0 and 1. NNSE = 1/(2 − NSE), which maps NSE = −1 to 1, NSE = 0 to 0.5, and NSE = −∞ to 0. R^2 indicates the proportion of variance in observed data explained by the model, with values closer to 1 reflecting stronger predictive capability. Q_0^i represents observed discharge; Q_s^i is the simulated discharge; $\overline{Q_0}$ is the mean observed discharge; $\overline{Q_s}$ is the mean simulated discharge, r is the Pearson correlation coefficient between observed and simulated values;

σ_s and σ_0 are the standard deviation of simulated and observed values, respectively; and n is the total number of observations.

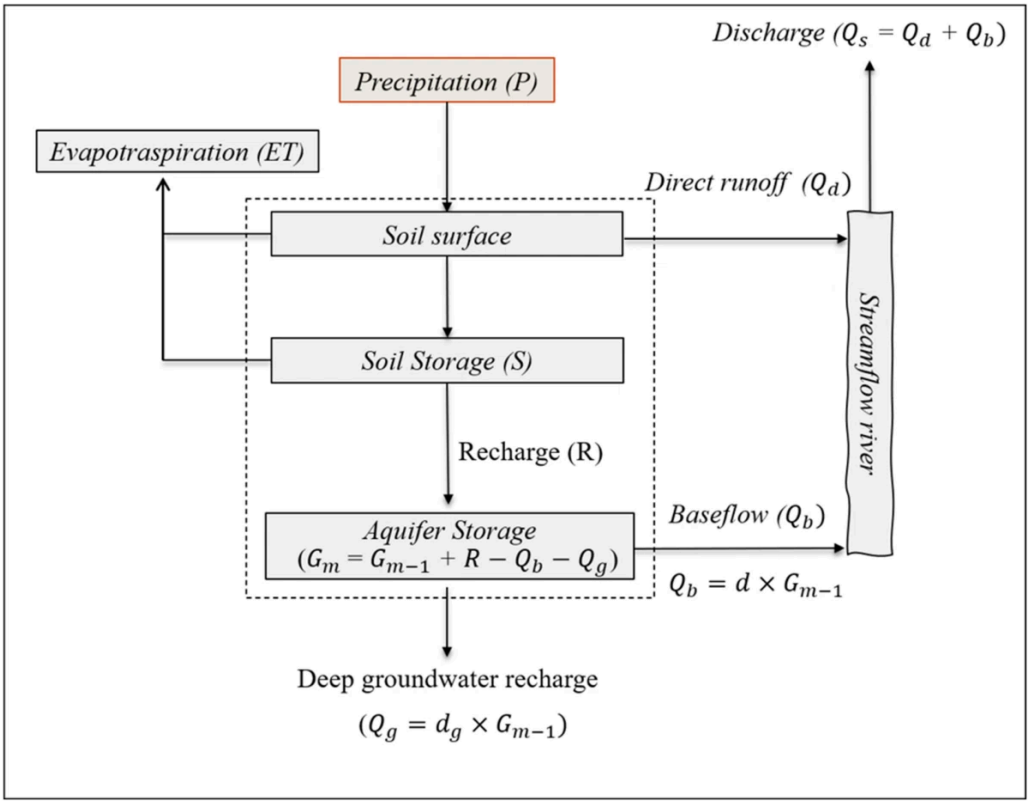


Figure 4. Adopted flowchart for water Dynamic Water Balance Model (DWBM) based on Budyko framework, showing precipitation (P) partitioning: direct runoff (Qd), actual evapotranspiration (ET), soil storage (S), aquifer storage contributing to base flow (Qb), and deep groundwater recharge (Qg).

Table 5. Metrics used for the evaluation of model performance.

Parameter	Expression	Range
RMSE	$\sqrt{\frac{\sum_{i=n}^{i}\left(Q_0^i - Q_s^i\right)^2}{n}}$	[0, ∞[
KGE	$1 - \sqrt{(r-1)^2 + \left(\frac{\sigma_s}{\sigma_0} - 1\right)^2 + \left(\frac{\overline{Q_s}}{\overline{Q_0}} - 1\right)^2}$	]−∞, 1]
NSE	$1 - \frac{\sum_{i=1}^{n}\left(Q_o^i - Q_S^i\right)^2}{\sum_{i=1}^{n}\left(Q_0^i - \overline{Q_0}\right)^2}$	]−∞, 1]
NNSE	$\frac{1}{2-NSE}$	[0, 1]
R2	$\left(\frac{\sum_{i=1}^{n}\left(Q_0^i Q_s^i\right) - \left(\sum_{i=1}^{n} Q_0^i\right)\left(\sum_{i=1}^{n} Q_s^i\right)}{\sqrt{n\sum_{i=1}^{n}\left(Q_0^i\right)^2 - \left(\sum_{i=1}^{n} Q_0^i\right)^2}\sqrt{n\sum_{i=1}^{n}\left(Q_s^i\right)^2 - \left(\sum_{i=1}^{n} Q_s^i\right)^2}}\right)^2$	[0, 1]

The model was calibrated by maximizing NNSE with an evolutionary algorithm implemented in Microsoft Excel®. At each step, the population size was set to 100 elements and the mutation rate to 0.075. The parameter search was interrupted when NNSE of the best 99% solutions differed by less than 0.01%. Parameters were constrained within the intervals reported in Table 6.

Table 6. Parameter ranges adopted during model calibration using the training dataset.

Smax (mm)	α_1 (–)	α_2 (–)	d (Month^{-1})	d_g (Month^{-1})
300–1200	0.01–0.99	0.01–0.99	0.1–2	0.1–1.0

To avoid overfitting and ensure reliable model results, the runoff data were split into two parts in chronological order: a calibration set and a validation set. The model was calibrated using the training dataset, while its performance was validated on the independent validation dataset. Hence, depending on the number of available measurement years, first years (70–75% of the data) were used to train the model, while the remaining 25–30% were used for validation.

2.5. Sensitivity Analysis

To explore the sensitivity of model output to parameter variations, the Monte Carlo sampling of the hydrologic parameters of the DWBM was carried out [48]. The analysis was performed using MATLAB R2026a (MathWorks Inc., Natick, MA, USA), where 50,000 parameter sets were randomly generated using the built-in *rand()* function to get uniform samples within the parameter ranges given in Table 6, suitable to visualize the variability of model performance around the best solution. The GoF between observed and simulated data was evaluated using NNSE. The resulting model performance index was assessed for all eight catchments using the available data, to evaluate how variations in individual parameters influence the simulated runoff response.

Moreover, a Sobol sensitivity analysis was carried out. It is a global variance-based method used to quantify the contribution of model parameters to the variability of model outputs. The Sobol method allows the decomposition of the total output variance into contributions associated with individual parameters and their interactions. Specifically, the following sensitivity indices were computed: the first-order indices (S_i), representing the direct effect of each parameter on the output; the total-order indices (ST_i), which account for both the direct effects and all higher-order interaction effects involving all parameters. The sampling scheme proposed by Saltelli et al. [49] was used to generate samples of model parameters, so as to have a similar amount of data as for the Monte-Carlo analysis (i.e., 49,152). The python library SALib (Sensitivity Analysis Library in Python 3.12, that uses Saltelli for samples) was used to do the Sobol sensitive analysis and a MATLAB code was used to run Budyko (both the codes are available in a public repository). For each parameter set, the model was run, producing an ensemble of outputs used to estimate the Sobol sensitivity indices. The results of the Sobol analysis allow the identification of the most influential parameters, detecting significant interaction effects among parameters, and reducing model complexity by focusing on the most relevant parameters. Parameters exhibiting high total-order indices (ST_i) are the primary drivers of model variability and, therefore, require accurate estimation. Conversely, parameters with low sensitivity can be assigned without significantly affecting model performance.

3. Results and Discussion

3.1. Budyko Model Calibration and Performance

In Table 7, the calibrated parameters show different degrees of variability among the eight catchments. The coefficient of variation indicates that dg (CV $\approx$ 38.8%) is the most variable parameter, followed by Smax (CV $\approx$ 27.7%) and d (CV $\approx$ 22.7%), whereas α_1 (CV $\approx$ 9.8%) shows the lowest variability, indicating a relatively consistent response across the catchments. The comparatively high variability in dg suggests greater differences in groundwater recession and storage–release characteristics among the catchments. Partic-

ularly, C3 behaves differently having relatively high α_2 and low d_g, indicating different hydrological responses compared to the other catchments. It is worth noting that the parameters of the gauged catchment C1 fall within the ranges for the ungauged catchments. This indicates that its calibrated parameterization does not represent an anomaly and is broadly consistent with the parameter variability obtained for ungauged catchments. In fact, catchment C1 was also calibrated with ERA5-Land runoff as the target, obtaining very similar model parameters as for the gauge-based calibration for α_2, d, and S_{max}; instead, α_1 and d_g are slightly different (Table 7). Therefore, despite the coarse spatial resolution of ERA5-Land runoff compared to the extension of some of the catchments, reanalysis-based runoff seems suitable for model calibration.

Table 7. Calibrated parameters of the conceptual hydrological model for each catchment. (* represents catchment C1 calibrated and validated based on ground discharge data.)

Catchment	S_{max} (mm)	α_1 (–)	α_2 (–)	d (Month^{-1})	d_g (Month^{-1})
C1 *	644	0.55	0.64	0.91	0.49
C1	632	0.65	0.68	0.89	0.41
C2	459	0.68	0.70	1.06	0.31
C3	647	0.61	0.78	1.12	0.13
C4	609	0.56	0.53	0.73	0.40
C5	766	0.56	0.59	0.69	0.63
C6	491	0.63	0.61	0.84	0.47
C7	1027	0.53	0.49	0.54	0.67
C8	557	0.51	0.58	0.91	0.45

The water-balance terms show marked variability among the eight catchments, with groundwater recharge exhibiting greater variability than runoff (see Table 8). C3 is the most distinctive catchment, exhibiting small groundwater recharge and runoff than the other catchments, as it receives the lowest precipitation while experiencing comparatively high evapotranspiration. In contrast, the highest runoff and ground water recharge are exhibited by C6 and C7, respectively.

Table 8. Mean annual water balance components for each catchment. The values refer to the entire observation period (training and validation) and have been obtained with the model calibrated based on the training set (* represents catchment C1 calibrated and validated based on ground discharge data).

Catchment.	Avg. Precipitation (mm/y)	Avg. ET (mm/y)	Avg. Deep Groundwater Recharge (mm/y)	Avg. Runoff (mm/y)
C1 *	1410	688	173	545
C2	1425	715	105	607
C3	1095	824	18	246
C4	1275	586	190	494
C5	1572	683	314	577
C6	1490	649	204	637
C7	1517	587	423	512
C8	1290	597	143	555

The model demonstrates consistently good performance across both the training and validation periods, with the performance metrics remaining broadly stable between the two phases as shown in Table 9. The differences between training and validation performance indicate that for many of the catchments the models do not overfit the training

dataset. However, the driest catchment, C3, exhibits the weakest validation performance, whereas C2 and C8 maintain strong performance during validation.

Table 9. Performance statistics of the model during the training and validation periods (r: Pearson correlation coefficient; RMSE: Root Mean Square Error; KGE: Kling–Gupta efficiency; NNSE: Normalized Nash–Sutcliffe Efficiency; Train.: training period; Val.: validation period).

Catchment	Periods		R		RMSE (mm)		NNSE		KGE	
	Train.	Valid.	Train.	Valid.	Train.	Valid.	Train.	Valid.	Train.	Valid.
C1 *	2003–2017	2018–2022	0.92	0.89	16.73	20.98	0.87	0.77	0.90	0.77
C2	2009–2019	2020–2023	0.92	0.97	23.02	13.60	0.87	0.92	0.91	0.91
C3	2009–2018	2019–2022	0.89	0.76	11.66	18.77	0.80	0.61	0.76	0.55
C4	2009–2018	2019–2022	0.89	0.90	16.75	17.21	0.83	0.83	0.84	0.79
C5	2008–2019	2020–2023	0.93	0.95	19.67	22.62	0.88	0.86	0.90	0.79
C6	2008–2019	2020–2023	0.92	0.94	25.95	28.97	0.86	0.84	0.90	0.75
C7	2008–2019	2020–2023	0.90	0.92	19.22	27.47	0.84	0.78	0.87	0.69
C8	2008–2019	2020–2023	0.94	0.95	17.29	17.44	0.90	0.89	0.91	0.87

Note: * represents catchment C1 calibrated and validated based on ground discharge data

Figure 5 compares the observed and simulated monthly runoff for four representative catchments selected to reflect the distinct hydrological conditions within the study area. The model successfully reproduced both the timing and magnitude of the seasonal discharge pattern, capturing the recurring winter spring peaks and the low-flow summer recession periods that characterize the study area's Mediterranean hydrological regime.

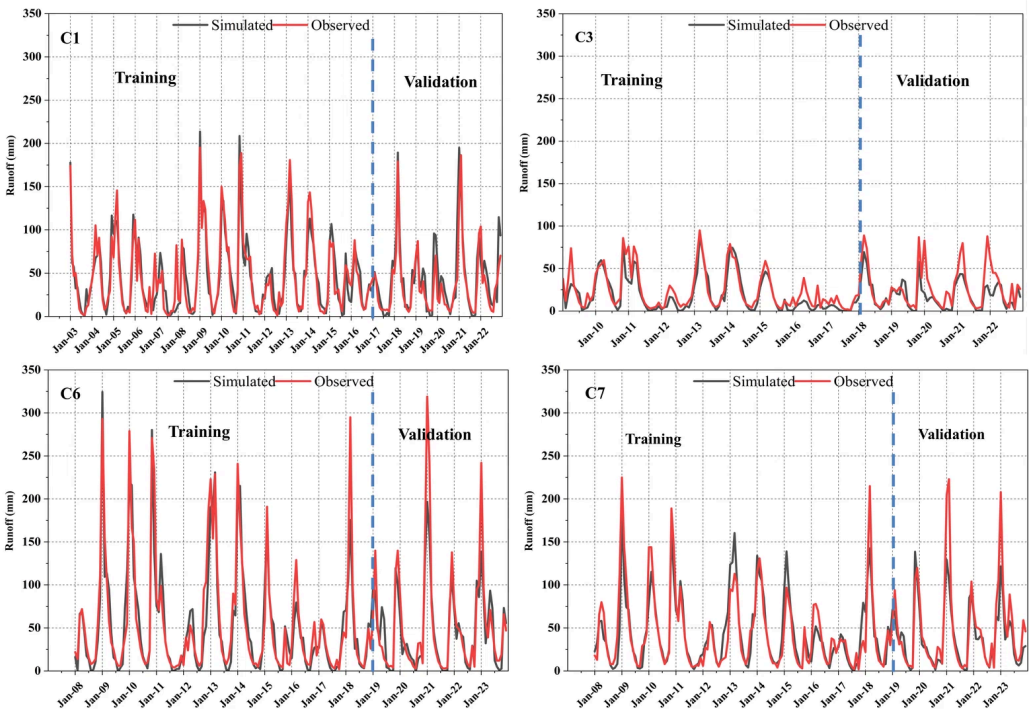


Figure 5. Comparison of observed and simulated monthly runoff during the training and validation periods for four representative catchments: C1 (gauged catchment), C3 (driest catchment), C6 (highest runoff), and C7 (highest groundwater recharge). The vertical dashed line separates the training and validation periods.

In the gauged catchment C1, the model reproduces the overall temporal variability and most runoff peaks satisfactorily during both the training and validation periods, although inconsistencies occur for some individual high-flow months. Overall, the monthly

hydrograph of the gauged catchment resembles those estimated from ERA5-Land, and the lumped model satisfactorily reproduces it with similar parameters. C3, the driest and hydrologically most distinctive catchment, shows reasonable agreement during training but a noticeable decline during validation, particularly in reproducing some runoff peaks. In C6, which exhibits the highest runoff, the model captures the timing and general magnitude of the major runoff events well, although some high-flow peaks show larger discrepancies, especially during the validation period. Similarly, for C7, characterized by the highest groundwater recharge, the simulated runoff generally follows the observed temporal dynamics, while some deviations in peak magnitude become evident during validation.

To check the consistency of the estimated water balance, Figure 6 shows the model's ability to reproduce evapotranspiration (ET) and soil water storage dynamics through a comparison with independent reference datasets (i.e., TerraClimate for ET and ERA5-Land for soil storage) for two representative catchments, C1 and C3. These catchments were selected to illustrate the overall behavior consistently observed across the studied catchments. Panels (a) and (b) compare simulated with TerraClimate ET for C1 and C3, respectively. In both catchments, the simulated ET closely reproduces the seasonal dynamics and temporal evolution of the TerraClimate estimates, capturing the characteristic Mediterranean regime of pronounced summer highest, approaching 100–160 mm, and low winter values of 20–50 mm. The timing of the seasonal transitions is also well represented. Agreement is generally better during winter and the spring and autumn transition periods; however, a systematic bias occurs during summer, when TerraClimate ET tends to exceed the simulated values, particularly in C3. This discrepancy suggests that the model underestimates peak summer ET because the simulated depletion of soil water under prolonged dry conditions constrains actual evapotranspiration.

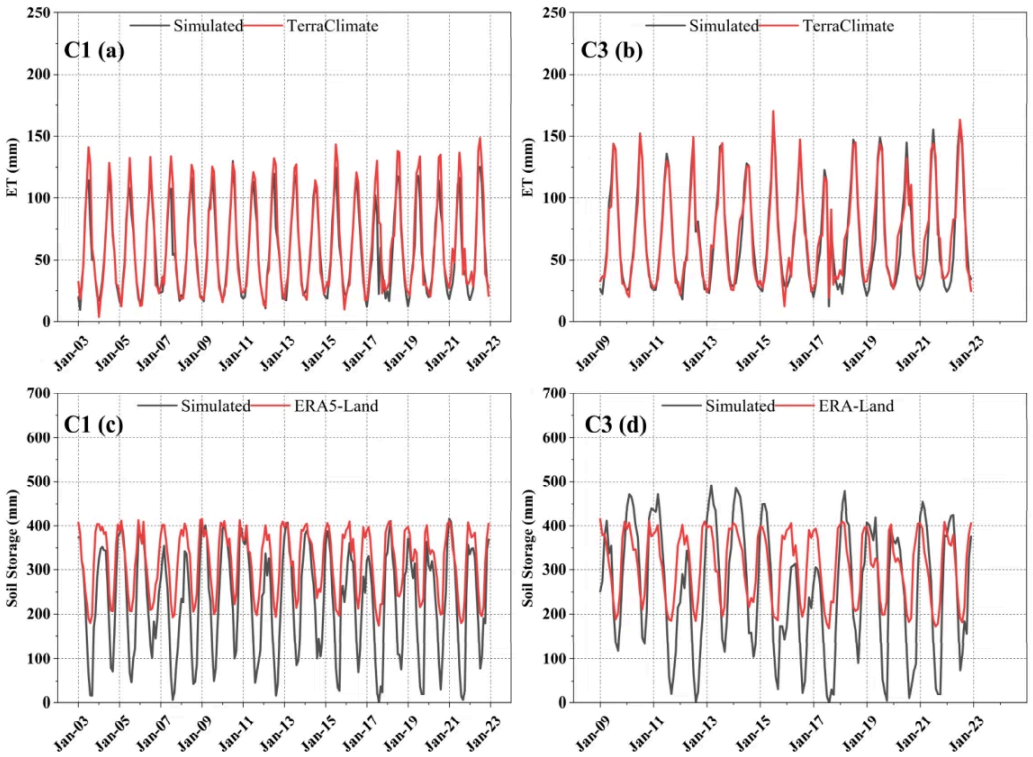


Figure 6. Comparison of simulated hydrological states against independent reference datasets for representative catchments C1 and C3. (**a**,**b**) Simulated evapotranspiration (ET) versus TerraClimate ET for C1 and C3, respectively, (**c**,**d**) Simulated soil storage versus ERA5-Land soil storage for C1 and C3, respectively. Catchments C1 and C3 are shown as representative examples of the consistent behavior observed across all studied catchments.

Panels (c) and (d) present the corresponding comparison of simulated and ERA5-Land soil storage for C1 and C3. Although both datasets reproduce the general seasonal wetting and drying cycle, notable differences are evident in the magnitude of the simulated fluctuations. ERA5-Land storage varies within a relatively narrow and damped range, approximately 150–400 mm, whereas the simulated storage exhibits a substantially larger seasonal amplitude, declining to near-zero values during the dry summer period and recovering rapidly to approximately 350–450 mm during wetter months. This stronger seasonal response, particularly the pronounced summer depletion, is consistent with the ET comparison in panels (a) and (b). The more rapid reduction in simulated soil water availability limits the amount of water available for evapotranspiration, thereby contributing to the underestimation of summer ET relative to TerraClimate. Overall, the results indicate that the model successfully captures the seasonal timing and general dynamics of both ET and soil water storage across the representative catchments, while simulating a more pronounced seasonal wetting–drying cycle than the reference reanalysis products, characterized by sharper summer depletion and more rapid recovery during wet periods.

3.2. Sensitivity Analysis

3.2.1. Monte Carlo Sampling

Having established the model's ability to reliably reproduce water balance components across all catchments, a Monte Carlo-based sensitivity analysis was conducted to quantify the influence of parameter uncertainty on simulated runoff. This analysis is particularly pertinent in the present study, given that, for most catchments, reanalysis-based discharge data rather than observed streamflow was used for model calibration and validation across the catchments. Since the choice of the runoff data source can influence the estimated parameter sets, it is important to assess how sensitive the simulated hydrological states are to this source of parameter uncertainty. Understanding this sensitivity provides confidence in the reliability of the calibrated parameters and, by extension, in their applicability where discharge observations are unavailable.

The sensitivity analysis, performed independently for each of the eight catchments, revealed consistent parameter sensitivity patterns across all catchments regardless of the runoff data source used for calibration. Importantly, the parameter values derived for the single gauged catchment fell within the range of variability observed among the ungauged catchments calibrated using ERA5-reanalysis runoff, indicating no clear systematic effect of the runoff data source on the resulting parameter estimates.

Figure 7 presents the scatter plots of NNSE against each of the five model parameters (Smax, α_1, α_2, d, d_g) for catchment C6, selected as a representative example, as the sensitivity patterns described below are broadly applicable across all catchments. The scatter plots illustrate the relationship between each parameter and the NNSE. Among the five parameters, Smax, α_1, α_2, and dg display a clearly defined dome-shaped distribution, with NNSE values rising toward the maximum within a relatively narrow parameter range and declining toward both extremes. This pattern with clear and well-constrained maxima is consistent across all catchments, with some exception for d_g, where a distinct maximum appears in some cases, and a broader less constrained response in others. In contrast, parameter d shows, in all cases, a broader, flatter distribution, with high NNSE values sustained across a wider range of the parameters and no sharply defined maximum.

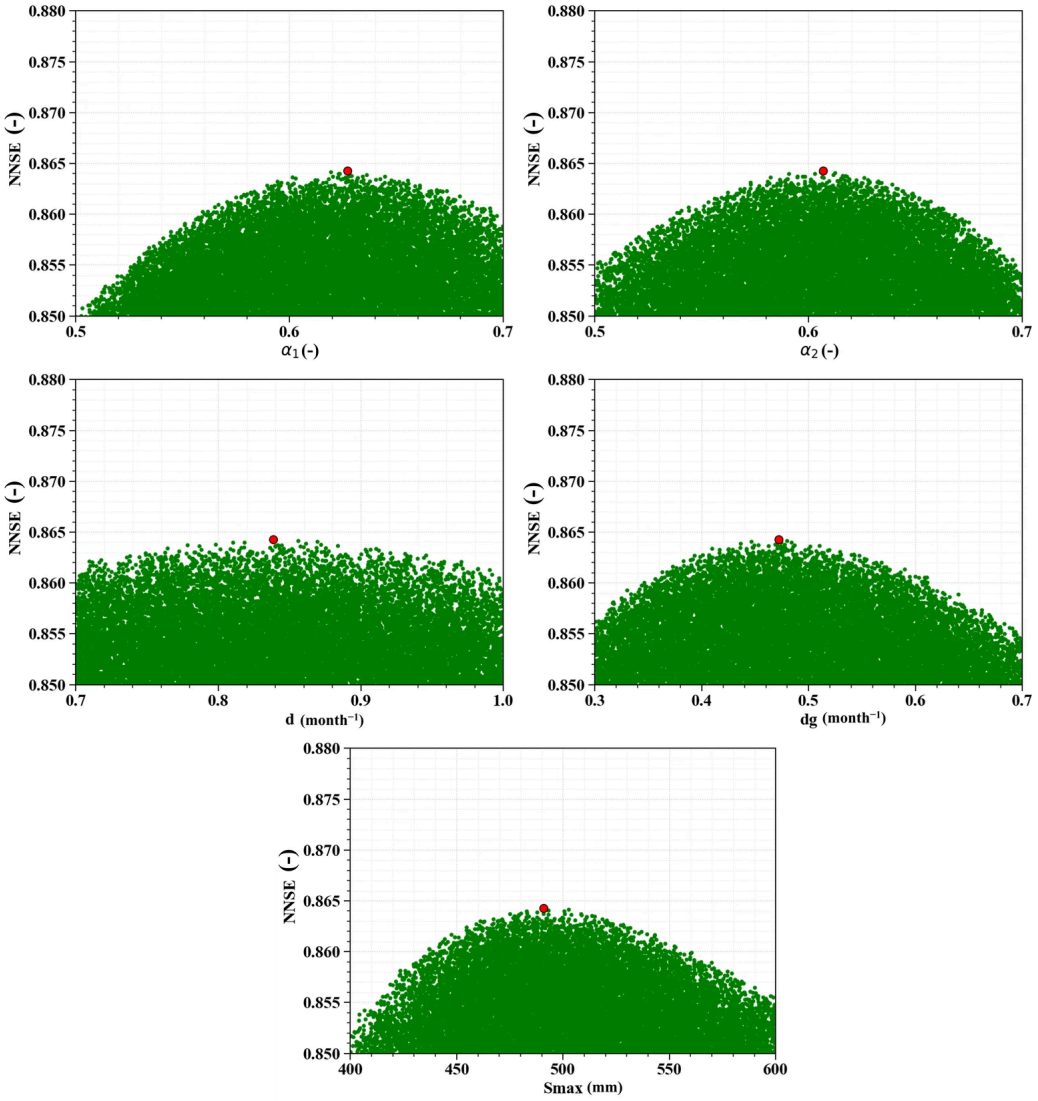


Figure 7. Model performance dependence on model parameters around the best parameter set (the example graphs refer to catchment C6). The red dot represents the best parameter set obtained through model calibration.

3.2.2. Sobol Global Sensitivity Analysis

The Sobol sensitivity results reported in Table 10 provide a quantitative assessment of the contribution of each parameter (S_{max}, α_1, α_2, d, d_g) to the variability of the model performance (NNSE), through both first order (S_1) and total-order (ST) indices.

Table 10. Sobol analysis test for studied catchments.

C. No	S_1					ST				
	Smax	α_1	α_2	d	d_g	Smax	α_1	α_2	d	d_g
C1	0.110	0.335	0.242	0.0544	0.022	0.201	0.450	0.404	0.180	0.065
C2	0.243	0.184	0.105	0.0557	0.024	0.432	0.391	0.305	0.222	0.108
C3	0.141	0.210	0.256	0.0718	0.026	0.245	0.312	0.473	0.240	0.086
C4	0.122	0.391	0.075	0.0115	0.023	0.375	0.612	0.279	0.109	0.070
C5	0.108	0.364	0.127	0.0504	0.007	0.327	0.556	0.321	0.168	0.033
C6	0.353	0.208	0.002	0.0077	0.033	0.644	0.463	0.220	0.044	0.064
C7	0.173	0.284	0.094	0.070	0.010	0.404	0.493	0.270	0.215	0.029
C8	0.022	0.189	0.116	0.123	0.108	0.123	0.281	0.286	0.434	0.345

Across the eight catchments, α_1 shows the strongest first-order effect (S_1 generally between 0.18 and 0.39), consistent with its direct control on runoff generation within the model structure. Its total-order indices remain consistently high (0.28–0.61) and in some cases quite larger than its first-order values, indicating that α_1's influence on model output variability is largely direct, also with a significant contribution from interactions with the other parameters.

Secondary influence parameters are S_{max} and α_2, though their relative importance varies markedly among catchments. S_{max} generally shows quite variable first-order sensitivity (S_1 between 0.02 and 0.35), yet its total-order indices are substantially larger (S_T between 0.12 and 0.64), indicating that S_{max} shows the largest influence on model performance through interactions with other parameters, rather than through its direct effect alone. α_2 shows a similar catchment-dependent pattern, characterized by generally small S_1 and high S_T, indicating that its influence on model output is expressed mainly through interactions rather than directly. Indeed, as clearly indicated by the structure of Fu's Equation (1) and the water balance Equations (2)–(5), α_1, S_{max}, and α_2 together control the water retained in the catchment and the consequent processes (i.e., soil storage, evapotranspiration, and groundwater recharge).

The parameters d and d_g generally show the lowest effect on model output variability, with both S_1 and S_T remaining comparatively small in most cases. This pattern is not universal; however, in C8, d and d_g attain the highest total-order indices in the entire dataset (S_T = 0.434 and 0.345, respectively), exceeding both α_1 and S_{max} for that catchment, indicating that groundwater-related processes can become the dominant control of simulated discharge in specific catchments.

4. Discussion

Figure 8 presents the Pearson correlation matrix between the five optimized model parameters and the set of catchment morphometric indices considered (Tables 1 and 2). As expected, correlated morphometric attributes show similar relationships with model parameters. Among all parameter and index combinations, mean elevation (E_{mean}) shows the strongest and most consistent associations, correlating negatively with α_1 (r = −0.66), α_2 (r = −0.79), and d (r = −0.62) and positively with d_g (r = 0.74). The Strahler order (U) similarly shows a strong positive relationship with d and α_2 and a strong negative relationship with d_g. The mean slope ($S_{\%}$) correlates strongly with d_g and moderately with α_2. In contrast, S_{max} shows only weak correlations with all standard morphometric indices, with its strongest association found instead with distance from the crater of Vesuvius (r = −0.56). Several indices, including the circularity ratio (R_c), relief ratio (R_h), and length of main stream, display consistently weak correlations with all parameters.

To further explore the physical controls of the calibrated parameters, the linear regression of each model parameter with its most strongly correlated morphometric index elevation is represented in Figure 9. Despite the small sample size (i.e., only eight catchments), the Fisher test reveals a statistically significant relationship for α_2 and dg (i.e., the p-value is 0.019 and 0.035, respectively). Differently, the relationships of α_1 and d with the Emean show only a marginally significant trend (the p-value is 0.088 and 0.10, respectively). In Figure 10, the power-law regression of S_{max} with D ($S_{max} = 2088.2D^{-0.45}$, R^2 = 0.45) also results as moderately significant (p-value = 0.067). All the relationships should be interpreted with caution (i.e., as exploratory) given the limited sample size (n = 8).

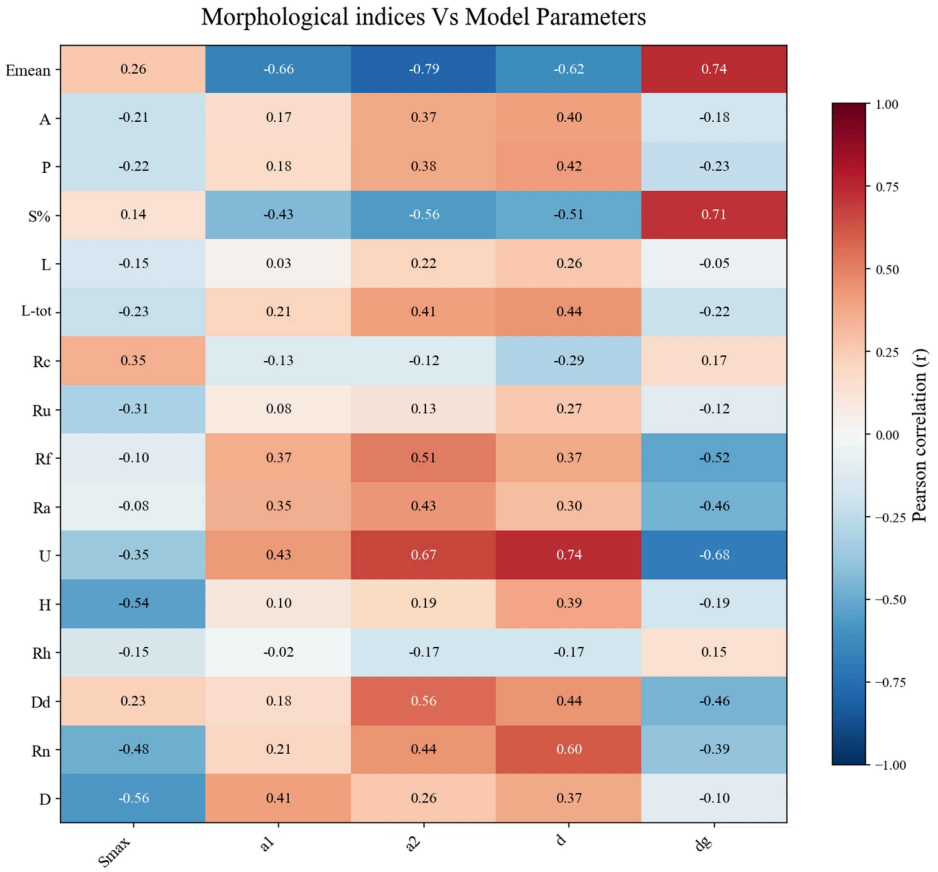


Figure 8. Pearson correlation matrix between catchment morphometric indices encompassing areal/shape (A, P, R_c, R_u, R_f, R_a), relief (E_{mean}, S%, H, R_h, R_n), and linear (U, D_d) aspects and the optimized parameters of the hydrological model (S_{max}, α_1, α_2, d, d_g) across the eight study catchments. Positive and negative correlations are indicated by red and blue shading, respectively, with color intensity proportional to the magnitude of the Pearson correlation coefficient (r).

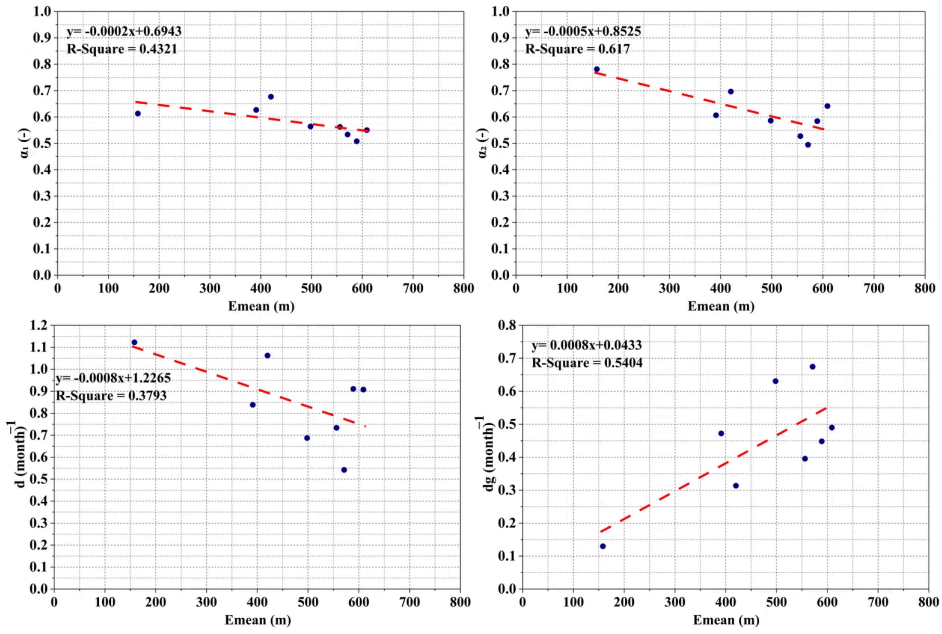


Figure 9. Linear regression of the calibrated model parameters α_1, α_2, d, and d_g against catchment mean elevation (E_{mean}) across the eight study catchments. Each panel shows the fitted linear trend line, regression equation, and coefficient of determination (R^2), illustrating the strength and direction of the parameter–elevation relationships.

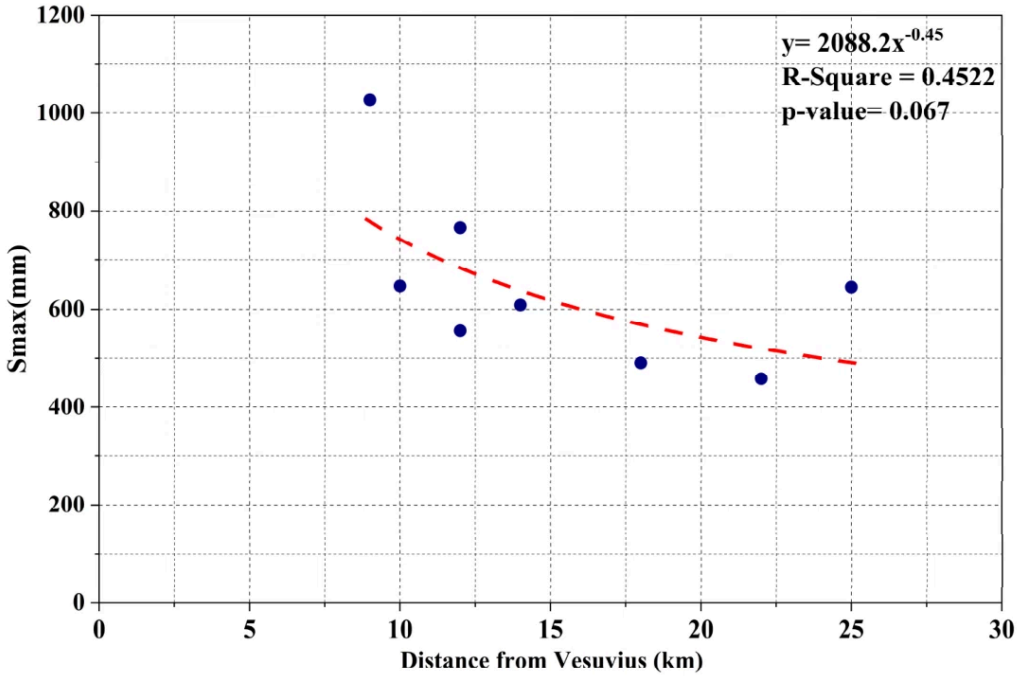


Figure 10. Relationship between maximum soil storage capacity (S_{max}) and distance D from Mount Vesuvius across the eight study catchments. Equation: $S_{max} = 2088.2D^{-0.45}$, $R^2 = 0.45$. The dashed line represents the fitted power-law trend line, indicating an inverse relationship between soil storage capacity and distance from the volcanic source.

The DWBM approach applied here is widely used in similar hydrological studies for its ability to capture the seasonal dynamics of catchment water fluxes [50,51]. Consistent with this framework, the study catchments show pronounced seasonal variability in their water balance, driven primarily by the seasonal contrast between precipitation and evapotranspiration: discharge peaks during the wet winter months, while summer ET dominates the water balance, suppressing both surface and subsurface flows. These findings are consistent with those reported by [16]. The model reproduced the seasonal dynamics of streamflow satisfactorily across catchments (Table 8), despite a tendency to underestimate peak flows during the wet months (December–April), especially in the months with the highest peaks. This indicates that model errors still contain a seasonal component, likely due to the limitation of the lumped modeling approach.

The calibrated parameter sets obtained across the eight catchments (Table 7) reveal a coherent picture of hydrological functioning despite the pronounced physiographic heterogeneity of the study area. The comparatively low variability of α_1, indicates that the runoff-generation mechanism operates in a relatively uniform manner across catchments. This behavior reflects the relatively homogeneous characteristics of the pyroclastic soil, and it is consistent with lumped-based frameworks in which the partitioning of precipitation into runoff is controlled by climatic aridity rather than catchment-specific attributes [40]. However, the higher variability found for dg and Smax demonstrates the catchments' ability to effectively retain water, reducing runoff while promoting soil storage and groundwater recharge before water is released to streams [52,53].

The distinct behavior of C3 (high α_2 and lower low d_g) is consistent with its water balance (Table 8), where the catchment receives the lowest precipitation while sustaining the highest evapotranspiration. This combination points to a system in which limited water availability constrains groundwater recharge, and it likely also explains the comparatively weaker validation performance obtained for C3 (Table 9; Figure 5). An important methodological outcome is that the parameter set obtained for the single gauged catchment

(C1) falls within the range of variability derived for the ungauged catchments calibrated against ERA5-Land reanalysis discharge, indicating that the discharge data source used for calibration does not introduce a systematic bias in the resulting parameters. This supports the regionalization strategy adopted here to use reanalysis-based discharge as a calibration target in the data-scarce Mediterranean region. Although ERA5-Land runoff is a modeled variable that is not subject to the assimilation of observations, the results obtained indicate its consistency within the hydrological balance of the studied catchments. However, the comparison with other gauged catchments would strengthen this conclusion. The model shows strong agreement with TerraClimate ET during winter and transitional seasons, confirming correct seasonal dynamics [54]. The summer ET deficit reflects the soil moisture limitation, corroborated by sharper simulated soil storage drawdown compared to ERA5-Land [55]. However, underestimated dry season soil moisture in the ERA5-Land dataset has been already reported in the study area, characterized by loose soils with high porosity (e.g., [23,56]). Hence, the simulated soil storage variability may be considered reliable.

The Monte Carlo scatter plots (Figure 7) and Sobol sensitivity indices (Table 10) together give a coherent picture of parameter identifiability. α_1 emerges as the dominant parameter, with well-constrained, dome-shaped NNSE responses and first-order indices close in magnitude to the total-order indices, indicating a strong, largely independent control of model performance, consistent with theoretical expectations that parameters governing the dominant flux term in a water balance model exert the strongest, least interaction-dependent influence [48,49]. α_2 plays a secondary but meaningful role: the larger gap between its first- and total-order indices suggests that its influence is expressed substantially and significantly through the interaction, most plausibly with α_1 and S_{max} via the coupled representation of evapotranspiration and soil storage.

In contrast, the low sensitivity and broader, flatter NNSE distributions with respect to d and dg point out the equifinality of modeled groundwater storage and release [30]. This does not mean that these parameters are hydrologically unimportant; rather, under a calibration framework based primarily on total streamflow, their effect on the aggregate discharge signal can be partly compensated by adjustments elsewhere in the parameter space, a well-documented challenge in constraining baseflow and deep percolation parameters from discharge data alone [30]. This suggests that future work incorporating field groundwater-level observations could reduce this uncertainty. The sensitivity to S_{max}, mostly through an interaction with other parameters, indicates a behavior already reported in other lumped and bucket-type models, where runoff and ET partitioning are more strongly governed by the shape parameters of the water balance curve than by the absolute storage capacity alone [57].

The correlation analysis (Figure 8) and the regression analysis against mean elevation (Figure 9) provide physically meaningful insight into the catchment-scale controls governing the calibrated parameters, offering a basis for regionalizing parameters to ungauged catchments. The consistent dependence of α_1, α_2, d, and d_g on the mean elevation is hydrologically interpretable: recharge of deep karst aquifers occurs in small high-elevation catchments, where actual evapotranspiration becomes smaller, as well as both direct runoff and baseflow compared to large catchments at a lower elevation [52,53]. This elevation-mediated control of runoff generation and storage dynamics is consistent with findings from other mountainous catchments in different environments [58].

Among the four elevation-dependent parameters, α_2 and d_g display the strongest linear relationships, suggesting that the nonlinearity of evapotranspiration partitioning and the deep groundwater recharge coefficient are the aspects of the water balance most robustly controlled by the catchment elevation. The comparatively weaker, though still physically consistent, relationships found for α_1 and d, likely reflect the additional influence of factors

not captured by elevation alone, such as land cover or localized geological heterogeneity, consistent with the moderate correlations that these parameters also show with the Strahler order and other morphometric indices (Figure 8).

The absence of any significant relationship between S_{max} and standard morphometric descriptors underscores an important structural distinction between this parameter and the others. Whereas α_1, α_2, d, and dg are closely tied to the catchment-scale topographic organization and drainage efficiency, S_{max} is governed primarily by the thickness and hydraulic characteristics of the soil and near-surface pyroclastic deposits, rather than by the catchment shape, relief, or drainage geometry. This explains why classical morphometric indices, which fundamentally describe the catchment shape and drainage network organization, fail to capture the variability in S_{max}. The improved, physically reasonable relationship obtained between S_{max} and the distance from the crater of Mount Vesuvius (Figure 10) is consistent with established volcanological evidence that pyroclastic thickness in the study area decreases with increasing distance from the eruptive vent [59–61], a pattern also documented more broadly for tephra fall deposits from explosive eruptions [62]. This provides a geologically grounded proxy for soil storage capacity where conventional morphometric indices are uninformative.

Taken together, these results indicate that the calibrated parameters are not merely empirical fitting coefficients but are, to a substantial degree, physically interpretable and predictable from catchment attributes. This outcome strengthens confidence in the internal consistency of the model structure and supports the use of elevation, and, for S_{max} specifically, the distance from the volcanic source, as physically justified predictors for extending the model to ungauged catchments in this volcanic Mediterranean area.

The monthly dynamics of the water balance estimated by the model provide valuable insights into potential susceptibility to geohazards. In particular, the model-predicted soil storage dynamics and runoff highlight the critical role of catchment water retention processes in governing the hydrological response, where progressive soil moisture accumulation can amplify surface runoff generation and increase the susceptibility of catchments to geohazards, including flash floods and debris flows, which are well documented and recurrent phenomena in the pyroclastic mantled slopes of the Campania region [63,64]. Moreover, the successful use of reanalysis data for ungauged catchments demonstrates the potential of remote sensing and gridded data in hydrological modeling. The morphometric analysis further revealed that catchment characteristics, such as elevation, play an important role in regulating water retention, runoff, and groundwater dynamics in this study area. Overall, these results highlight that the proposed study can be applied in regions with similar physiographic characteristics for water balance assessment.

Limitations of the Model

Despite providing useful insights into catchment hydrological behavior, several limitations should be acknowledged. First, the analysis was conducted on a relatively small number of catchments, which may restrict the generalization of the relationships between morphometric indices and model parameters. Second, for ungauged catchments, runoff observations were derived from a reanalysis dataset, raising two issues: the use of a model result (although reanalyzed with observed data assimilation) to calibrate another model; the coarseness of the gridded reanalysis dataset. Regarding the first issue, in ungauged catchments, no other options exist, and the results of this study seem to indicate that the assimilation of meteorological observations allows a reliable estimate of surface runoff (which is not assimilated). Regarding the second issue, although a lumped modeling approach was adopted, which does not require spatially detailed information, the coarseness of the reanalysis data may still limit the reliability of the results, especially for small catchments.

Then, a comparison with more gauged catchments, also in other geomorphological contexts, may allow an assessment of to what extent the results of this study can be generalized. Finally, it is worth noticing that the pyroclastic deposit thickness may change in quite active volcanic areas. However, in the case of Campania, where volcanic complexes are indeed still active, big eruptions that cause the deposition of significant amounts of air-fall pyroclastic materials are relatively infrequent. Only four eruptions happened in the last four thousand years, and the last one occurred more than 1600 years ago. Therefore, we have not considered the possible dynamic variability of soil thickness in the discussion.

5. Conclusions

This study demonstrates that the Budyko-based Dynamic Water Balance Model (DWBM) satisfactorily reproduces the monthly water balance dynamics of eight pyroclastic catchments in Campania using ground-based and reanalysis-based data. While peak discharge was occasionally underestimated during wet months, the model captured the overall seasonal patterns of water balance components. Independent comparisons with TerraClimate ET and ERA5-Land soil storage further supported the physical consistency of the simulations. The results indicate that, in the study area, surface runoff estimated by a reanalysis product (i.e., ERA5-Land) can be an acceptable surrogate for measured runoff in ungauged catchments. Sensitivity analysis identified α_1 as the dominant parameter controlling model performance, whereas groundwater-related parameters showed greater uncertainty. The calibrated model parameters exhibited meaningful relationships with catchment characteristics, with mean elevation explaining variations in α_1, α_2, d, and d_g, while S_{max} was related to distance from the Mount Vesuvius volcano. Future work will investigate if the water balance components may be useful to improve rainfall-induced geohazard assessments at a catchment scale in data-scarce Mediterranean environments. In particular, the potential use of catchment hydrological variables, such as soil water storage, to inform hydrometeorological thresholds for landslide occurrence will be explored. However, the suitability of thresholds based only on soil storage may be limited in catchments characterized by large groundwater recharge, where subsurface water redistribution may lead to different hydrological responses of slopes.

Author Contributions: M.A.: Conceptualization, Methodology, Formal analysis, Data curation, Writing -original draft, P.M.: Conceptualization, Methodology, Formal analysis, Writing – review and editing, R.G.: Super-vision, Conceptualization, Methodology, Writing - review and editing, Funding acquisition. All authors have read and agreed to the published version of the manuscript.

Funding: This study was carried out within the RETURN Extended Partnership and received funding from the European Union Next-Generation EU (National Recovery and Resilience Plan NRRP, Mission 4, Component 2, Investment 1.3—D.D. 1243 2/8/2022, PE0000005).

Data Availability Statement: Data will be made available on reasonable request from the first author. The codes used for running the sensitivity analyses are available at https://github.com/Aleem-debug/Budyko-DWBM-Sensitivity-Analysis, accessed on 18 October 2026.

Acknowledgments: This research is part of the PhD project of Muhammad Aleem entitled "Hydrometeorological approach for geo-hydrologic hazard assessment in small catchments" within the Doctoral Course "Science and Engineering for the Environment and the Sustainability" of Università degli Studi della Campania "Luigi Vanvitelli".

Conflicts of Interest: The authors declare no conflicts of interest.

References

1. Refsgaard, J.C.; Stisen, S.; Koch, J. Hydrological process knowledge in catchment modelling—Lessons and perspectives from 60 years development. *Hydrol. Process.* **2022**, *36*, e14463. [CrossRef]
2. Pandi, D.; Kothandaraman, S.; Kuppusamy, M. Hydrological models: A review. *Int. J. Hydrol. Sci. Technol.* **2021**, *12*, 223–242. [CrossRef]
3. Pechlivanidis, I.G.; Jackson, B.M.; Mcintyre, N.R.; Wheater, H.S. Catchment Scale Hydrological Modelling: A Review of Model Types, Calibration Approaches and Uncertainty Analysis Meth-Ods in the Context of Recent Developments in Technology and Applications. 2011. Available online: https://www.cabidigitallibrary.org/doi/full/10.5555/20123086769 (accessed on 17 September 2026).
4. Chowdhury, S.T.; Yasmin, F.; Tanni, M.M.P.; Rahman, M.; Sarwar, H.; Tin, T.T. A systematic review of flood prediction (2018–2025): Flood categories, input features, and Machine Learning, Deep Learning and hybrid approaches. *Watershed Ecol. Environ.* **2026**, *8*, 185–207. [CrossRef]
5. Mosavi, A.; Ozturk, P.; Chau, K. Flood Prediction Using Machine Learning Models: Literature Review. *Water* **2018**, *10*, 1536. [CrossRef]
6. Okiria, E.; Okazawa, H.; Noda, K.; Kobayashi, Y.; Suzuki, S.; Yamazaki, Y. A Comparative Evaluation of Lumped and Semi-Distributed Conceptual Hydrological Models: Does Model Complexity Enhance Hydrograph Prediction? *Hydrology* **2022**, *9*, 89. [CrossRef]
7. Vansteenkiste, T.; Tavakoli, M.; Van Steenbergen, N.; De Smedt, F.; Batelaan, O.; Pereira, F.; Willems, P. Intercomparison of five lumped and distributed models for catchment runoff and extreme flow simulation. *J. Hydrol.* **2014**, *511*, 335–349. [CrossRef]
8. Vilaseca, F.; Narbondo, S.; Chreties, C.; Castro, A.; Gorgoglione, A. A comparison between lumped and distributed hydrological models for daily rainfall-runoff simulation. *IOP Conf. Ser. Earth Environ. Sci.* **2021**, *958*, 012016. [CrossRef]
9. Chiew, F.H.S. Lumped Conceptual Rainfall-Runoff Models and Simple Water Balance Methods: Overview and Applications in Ungauged and Data Limited Regions. *Geogr. Compass* **2010**, *4*, 206–225. [CrossRef]
10. Wang, C.; Wang, S.; Fu, B.; Zhang, L. Advances in hydrological modelling with the Budyko framework: A review. *Prog. Phys. Geogr.* **2016**, *40*, 409–430. [CrossRef]
11. Jaramillo, F.; Piemontese, L.; Berghuijs, W.; WAng-Erlandsson, L.; Greve, P. Most River Basins will Follow their Budyko Curves under Global Warming. In Proceedings of the EGU General Assembly Conference Abstracts, Vienna, Austria; Online, 23–27 May 2022; p. EGU22-11224. [CrossRef]
12. Zhang, L.; Potter, N.; Hickel, K.; Zhang, Y.; Shao, Q. Water balance modeling over variable time scales based on the Budyko framework—Model development and testing. *J. Hydrol.* **2008**, *360*, 117–131. [CrossRef]
13. Budyko, M.I. The Heat Balance of the Earth's Surface. *Sov. Geogr.* **1961**, *2*, 3–13. [CrossRef]
14. Sun, D.; Gao, G.; Wu, L.; Cui, Y.; Ma, Y.; Wang, X.; Shu, H. Attribution of runoff change and evaluation of water-balance closure based on a Budyko combined method of zonation, connectivity, and closure: A case study of the Xihan River basin in Northwest China. *Ecol. Indic.* **2026**, *183*, 114623. [CrossRef]
15. Zhou, D.; Zheng, C.; Jia, L.; Menenti, M. Partitioning Green and Blue Evapotranspiration by Improving Budyko Equation Using Remote Sensing Observations in an Arid/Semi-Arid Inland River Basin in China. *Remote Sens.* **2025**, *17*, 612. [CrossRef]
16. Marino, P.; Comegna, L.; Damiano, E.; Olivares, L.; Greco, R. Monitoring the Hydrological Balance of a Landslide-Prone Slope Covered by Pyroclastic Deposits over Limestone Fractured Bedrock. *Water* **2020**, *12*, 3309. [CrossRef]
17. D'Ippolito, A.; Lupiano, V.; Rago, V.; Terranova, O.G.; Iovine, G. Triggering of Rain-Induced Landslides, with Applications in Southern Italy. *Water* **2023**, *15*, 277. [CrossRef]
18. Fusco, F.; Bordoni, M.; Tufano, R.; Vivaldi, V.; Meisina, C.; Valentino, R.; Bittelli, M.; De Vita, P. Hydrological regimes in different slope environments and implications on rainfall thresholds triggering shallow landslides. *Nat. Hazards* **2022**, *114*, 907–939. [CrossRef]
19. Rianna, G.; Reder, A.; Mercogliano, P.; Pagano, L. Evaluation of Variations in Frequency of Landslide Events Affecting Pyroclastic Covers in Campania Region under the Effect of Climate Changes. *Hydrology* **2017**, *4*, 34. [CrossRef]
20. Greco, R.; Marino, P.; Santonastaso, G.F.; Damiano, E. Interaction between Perched Epikarst Aquifer and Unsaturated Soil Cover in the Initiation of Shallow Landslides in Pyroclastic Soils. *Water* **2018**, *10*, 948. [CrossRef]
21. Cascini, L.; Sorbino, G.; Cuomo, S.; Ferlisi, S. Seasonal effects of rainfall on the shallow pyroclastic deposits of the Campania region (southern Italy). *Landslides* **2014**, *11*, 779–792. [CrossRef]
22. Greco, R.; Marino, P.; Bogaard, T.A. Recent advancements of landslide hydrology. *WIREs Water* **2023**, *10*, e1675. [CrossRef]
23. Roman Quintero, D.C.; Marino, P.; Abdullah, A.; Santonastaso, G.F.; Greco, R. Large-scale assessment of rainfall-induced landslide hazard based on hydrometeorological information: Application to Partenio Massif (Italy). *Nat. Hazards Earth Syst. Sci.* **2025**, *25*, 2679–2698. [CrossRef]
24. Del Rio, A.A.; Ramirez, A.I.; Sanchez, M.A. The Role of Topography on the Shape of Unit Hydrographs in Small and Medium Sized Watersheds through a Physical Model. *Water* **2020**, *12*, 2270. [CrossRef]

25. Raja Shekar, P.; Mathew, A. Morphometric analysis of watersheds: A comprehensive review of data sources, quality, and geospatial techniques. *Watershed Ecol. Environ.* **2024**, *6*, 13–25. [CrossRef]
26. Zhang, J.; Dai, Q.; Nanding, N.; Han, D. Exploring the effect of catchment morphology on streamflow characteristics with virtual experiments. *J. Hydrol.* **2022**, *608*, 127606. [CrossRef]
27. Capozzi, V.; Annella, C.; Budillon, G. Classification of daily heavy precipitation patterns and associated synoptic types in the Campania Region (southern Italy). *Atmos. Res.* **2023**, *289*, 106781. [CrossRef]
28. Roman Quintero, D.C.; Damiano, E.; Olivares, L.; Greco, R. Mechanical and hydraulic properties of unsaturated layered pyroclastic ashes in landslide-prone areas of Campania (Italy). *Bull. Eng. Geol. Environ.* **2024**, *83*, 291. [CrossRef]
29. Del Soldato, D.; Pazzi, V.; Segoni, S.; De Vita, P.; Tofani, V.; Moretti, S. Spatial modeling of pyroclastic cover deposit thickness (depth to bedrock) in peri-volcanic areas of Campania (southern Italy). *Earth Surf. Process. Landf.* **2018**, *43*, 1757–1767. [CrossRef]
30. Beven, K.J. *Rainfall-Runoff Modelling: The Primer*; John Wiley & Sons: Hoboken, NJ, USA, 2012; ISBN 978-0-470-71459-1.
31. Rai, R.K.; Ojha, C.S.P.; Singh, V.P. *Handbook of Applied Hydrologic and Water Resources Engineering*; CRC Press: Boca Raton, FL, USA, 2025. [CrossRef]
32. Garzon, L.F.L.; Johnson, M.F.; Mount, N.; Gomez, H. Exploring the effects of catchment morphometry on overland flow response to extreme rainfall using a 2D hydraulic-hydrological model (IBER). *J. Hydrol.* **2023**, *627*, 130405. [CrossRef]
33. Reddy, P.J.R. *A Text Book of Hydrology*; Firewall Media: Almere, The Netherlands, 2005; ISBN 978-81-7008-099-2.
34. Chorley, R.; Horton, R.E. 1945: Erosional development of streams and their drainage basins: Hydrophysical approach to quantitative morphology. *Prog. Phys. Geogr. Earth Environ.* **1995**, *19*, 533–554. [CrossRef]
35. Horton, R.E. Erosional Development of Streams and Their Drainage Basins; Hydrophysical Approach to Quan-Titative Morphology. *GSA Bull.* **1945**, *56*, 275–370. [CrossRef]
36. Melton, M.A. "An Analysis of the Relations Among Elements of Climate, Surface Properties, and Geomorphol-Ogy," Art. No. CUTR11, Sep. 1957. Available online: https://archive.org/details/DTIC_AD0148373/page/n13/mode/2up (accessed on 5 March 2026).
37. Terink, W.; Leijnse, H.; van den Eertwegh, G.; Uijlenhoet, R. Spatial resolutions in areal rainfall estimation and their impact on hydrological simulations of a lowland catchment. *J. Hydrol.* **2018**, *563*, 319–335. [CrossRef]
38. Butler, T.; Graham, L.; Estep, D.; Dawson, C.; Westerink, J.J. Definition and solution of a stochastic inverse problem for the Manning's *n* parameter field in hydrodynamic models. *Adv. Water Resour.* **2015**, *78*, 60–79. [CrossRef]
39. Hwang, J.; Devineni, N. An Improved Zhang's Dynamic Water Balance Model Using Budyko-Based Snow Representation for Better Streamflow Predictions. *Water Resour. Res.* **2022**, *58*, e2021WR030203. [CrossRef]
40. Zhang, L.; Dawes, W.R.; Walker, G.R. Response of mean annual evapotranspiration to vegetation changes at catchment scale. *Water Resour. Res.* **2001**, *37*, 701–708. [CrossRef]
41. Donohue, R.J.; Roderick, M.L.; McVicar, T.R. On the importance of including vegetation dynamics in Budyko's hydrological model. *Hydrol. Earth Syst. Sci.* **2007**, *11*, 983–995. [CrossRef]
42. Calder, I.R. Water use by forests, limits and controls. *Tree Physiol.* **1998**, *18*, 625–631. [CrossRef]
43. Fu, B.P. On the calculation of the evaporation from land surface. *Sci. Atmos. Sin.* **1981**, *5*, 23. Available online: https://cir.nii.ac.jp/crid/1371694364625911058 (accessed on 7 March 2026).
44. Milly, P.C.D.; Dunne, K.A. Macroscale water fluxes 2. Water and energy supply control of their interannual variability. *Water Resour. Res.* **2002**, *38*, 24-1–24-9. [CrossRef]
45. Sankarasubramanian, A.; Vogel, R.M. Annual hydroclimatology of the United States. *Water Resour. Res.* **2002**, *38*, 19-1–19-12. [CrossRef]
46. Gupta, H.V.; Kling, H.; Yilmaz, K.K.; Martinez, G.F. Decomposition of the mean squared error and NSE performance criteria: Implications for improving hydrological modelling. *J. Hydrol.* **2009**, *377*, 80–91. [CrossRef]
47. Nash, J.E.; Sutcliffe, J.V. River flow forecasting through conceptual models part I—A discussion of principles. *J. Hydrol.* **1970**, *10*, 282–290. [CrossRef]
48. Chatzivasileiadis, T. Quasi-Monte Carlo application in CGE systematic sensitivity analysis. *Appl. Econ. Lett.* **2018**, *25*, 1521–1526. [CrossRef]
49. Saltelli, A.; Ratto, M.; Andres, T.; Campolongo, F.; Cariboni, J.; Gatelli, D.; Saisana, M.; Tarantola, S. *Global Sensitivity Analysis: The Primer*; John Wiley & Sons: Hoboken, NJ, USA, 2008; ISBN 978-0-470-72517-7.
50. Ning, Z.; Zhang, J.; Wu, N.; Hashemi, H.; Jaramillo, F.; Naghibi, A.; Xie, K.; Ruan, Y.; Liu, C.; Wang, G.; et al. Multi-model simulation performance of monthly water balance models for global catchments: Thresholds and structural sensitivity. *J. Hydrol.* **2026**, *667*, 134852. [CrossRef]
51. Zhang, X.; Dong, Q.; Zhang, Q.; Yu, Y. A unified framework of water balance models for monthly, annual, and mean annual timescales. *J. Hydrol.* **2020**, *589*, 125186. [CrossRef]
52. Allocca, V.; Manna, F.; De Vita, P. Estimating annual groundwater recharge coefficient for karst aquifers of the southern Apennines (Italy). *Hydrol. Earth Syst. Sci.* **2014**, *18*, 803–817. [CrossRef]

53. Fusco, F.; Allocca, V.; De Vita, P. Hydro-geomorphological modelling of ash-fall pyroclastic soils for debris flow initiation and groundwater recharge in Campania (southern Italy). *CATENA* **2017**, *158*, 235–249. [CrossRef]
54. Abatzoglou, J.T.; Dobrowski, S.Z.; Parks, S.A.; Hegewisch, K.C. TerraClimate, a high-resolution global dataset of monthly climate and climatic water balance from 1958–2015. *Sci. Data* **2018**, *5*, 170191. [CrossRef]
55. Muñoz-Sabater, J.; Dutra, E.; Agustí-Panareda, A.; Albergel, C.; Arduini, G.; Balsamo, G.; Boussetta, S.; Choulga, M.; Harrigan, S.; Hersbach, H.; et al. ERA5-Land: A state-of-the-art global reanalysis dataset for land applications. *Earth Syst. Sci. Data* **2021**, *13*, 4349–4383. [CrossRef]
56. Reder, A.; Rianna, G. Exploring ERA5 reanalysis potentialities for supporting landslide investigations: A test case from Campania Region (Southern Italy). *Landslides* **2021**, *18*, 1909–1924. [CrossRef]
57. Pianosi, F.; Wagener, T. Understanding the time-varying importance of different uncertainty sources in hydrological modelling using global sensitivity analysis. *Hydrol. Process.* **2016**, *30*, 3991–4003. [CrossRef]
58. Zuecco, G.; Penna, D.; Borga, M. Runoff generation in mountain catchments: Long-term hydrological monitoring in the Rio Vauz Catchment, Italy. *CIG* **2018**, *44*, 397–428. [CrossRef]
59. De Vita, P.; Agrello, D.; Ambrosino, F. Landslide susceptibility assessment in ash-fall pyroclastic deposits surrounding Mount Somma-Vesuvius: Application of geophysical surveys for soil thickness mapping. *J. Appl. Geophys.* **2006**, *59*, 126–139. [CrossRef]
60. Rolandi, G.; Munno, R.; Postiglione, I. The A.D. 472 eruption of the Somma volcano. *J. Volcanol. Geotherm. Res.* **2004**, *129*, 291–319. [CrossRef]
61. Sulpizio, R.; Mele, D.; Dellino, P.; Volpe, L.L. A complex, Subplinian-type eruption from low-viscosity, phonolitic to tephri-phonolitic magma: The AD 472 (Pollena) eruption of Somma-Vesuvius, Italy. *Bull. Volcanol.* **2005**, *67*, 743–767. [CrossRef]
62. Pyle, D.M. The thickness, volume and grainsize of tephra fall deposits. *Bull. Volcanol.* **1989**, *51*, 1–15. [CrossRef]
63. Napolitano, E.; Fusco, F.; Baum, R.L.; Godt, J.W.; De Vita, P. Effect of antecedent-hydrological conditions on rainfall triggering of debris flows in ash-fall pyroclastic mantled slopes of Campania (southern Italy). *Landslides* **2016**, *13*, 967–983. [CrossRef]
64. Santangelo, N.; Forte, G.; De Falco, M.; Chirico, G.B.; Santo, A. New insights on rainfall triggering flow-like landslides and flash floods in Campania (Southern Italy). *Landslides* **2021**, *18*, 2923–2933. [CrossRef]

Disclaimer/Publisher's Note: The statements, opinions and data contained in all publications are solely those of the individual author(s) and contributor(s) and not of MDPI and/or the editor(s). MDPI and/or the editor(s) disclaim responsibility for any injury to people or property resulting from any ideas, methods, instructions or products referred to in the content.